

On the spreading behavior of a droplet on a circular cylinder using the lattice Boltzmann method

Fan Yang(杨帆), Hu Jin(金虎), Mengyao Dai(戴梦瑶)

Citation: Chin. Phys. B, 2024, 33 (**6**): 064702. DOI: 10.1088/1674-1056/ad3b7f
Journal homepage: http://cpb.iphy.ac.cn; http://iopscience.iop.org/cpb

What follows is a list of articles you may be interested in

Bacterial turbulence in gradient confinement

Ningzhe Yan(颜宁哲), Chenliang Xie(谢晨亮), Hao Luo(罗昊), Yanan Liu(刘亚楠), and Guangyin Jing(经光银)
Chin. Phys. B, 2023, 32 (**11**): 114704. DOI: 10.1088/1674-1056/acea6d

Discussion on interface deformation and liquid breakup mechanism in vapor-liquid two-phase flow

Xiang An(安祥), Bo Dong(董波), Ya-Jin Zhang(张雅瑾), and Xun Zhou(周训)
Chin. Phys. B, 2023, 32 (**9**): 094702. DOI: 10.1088/1674-1056/acc78e

Dynamic evolution of low-viscosity fuel particle distribution driven by constant flow

Zhong-Kun Yang(杨仲坤), Gao-Jun An(安高军), Xi-Meng Xu(徐曦萌), Zhe Zheng(郑哲), Yong-Xu Wang(王永旭), Li-Feng Xie(解立峰), Dan Zhang(张丹), and Bin Li(李斌)
Chin. Phys. B, 2023, 32 (**7**): 074701. DOI: 10.1088/1674-1056/acc8c2

Drop impact on substrates with heterogeneous stiffness

Yang Cheng(成阳), Jian-Gen Zheng(郑建艮), Chen Yang(杨晨), Song-Lei Yuan(袁松雷), Guo Chen(陈果), and Li-Yu Liu(刘雳宇)
Chin. Phys. B, 2022, 31 (**8**): 084702. DOI: 10.1088/1674-1056/ac5c33

Crown evolution kinematics of a camellia oil droplet impacting on a liquid layer

Zhongyu Shi(石中玉), Guanqing Wang(王关晴), Xiangxiang Chen(陈翔翔), Lu Wang(王路), Ning Ding(丁宁), and Jiangrong Xu(徐江荣)
Chin. Phys. B, 2022, 31 (**5**): 054701. DOI: 10.1088/1674-1056/ac46c1

On the spreading behavior of a droplet on a circular cylinder using the lattice Boltzmann method

Fan Yang(杨帆)[1,2,†], Hu Jin(金虎)[1], and Mengyao Dai(戴梦瑶)[1]

[1] *School of Energy and Power Engineering, University of Shanghai for Science and Technology, Shanghai* 200093, *China*
[2] *Shanghai Key Laboratory of Multiphase Flow and Heat Transfer in Power Engineering, Shanghai* 200093, *China*

(Received 12 December 2023; revised manuscript received 8 March 2024; accepted manuscript online 7 April 2024)

The study of a droplet spreading on a circular cylinder under gravity was carried out using the pseudo-potential lattice Boltzmann high-density ratios multiphase model with a non-ideal Peng–Robinson equation of state. The calculation results indicate that the motion of the droplet on the cylinder can be divided into three stages: spreading, sliding, and aggregating. The contact length and contact time of a droplet on a cylindrical surface can be affected by factors such as the wettability gradient of the cylindrical wall, the Bond number, and droplet size. Furthermore, phase diagrams showing the relationship between Bond number, cylinder wall wettability gradient, and contact time as well as maximum contact length for three different droplet sizes are given. A theoretical foundation for additional research into the heat and mass transfer process between the droplet and the cylinder can be established by comprehending the variable rules of maximum contact length and contact time.

Keywords: lattice Boltzmann methods, droplet, circular cylinder, wettability gradient

PACS: 47.61.Jd, 61.30.Pq, 47.11.Qr, 02.60.Cb **DOI:** 10.1088/1674-1056/ad3b7f

1. Introduction

It is a common phenomenon for liquid droplets coming into contact with solid surfaces, such as droplet falling onto plant leaves, drug coating, metallurgy, ink-jet printing, and internal combustion engines.[1] This phenomenon is often accompanied by heat and mass transfer processes between the droplets and the solid. In everyday life, when encountering scenarios involving the contact between droplets and solids accompanied by heat and mass transfer processes, people often have two types of demands. One is to control the accelerated detachment of droplets from the solid surface, reducing the contact time and area between the droplets and the solid surface, thereby weakening the heat and mass transfer between the droplets and the solid. For example, during high-intensity exercise, specially designed patterns can be fabricated on the outer surface of moisture-wicking fabrics to achieve rapid sweat removal for fast drying.[2] Additionally, in air condensation water harvesting applications, rapidly driving the condensed droplets to move in a specific direction accelerates droplet nucleation and increases water collection efficiency.[3] In contrast, in some scenarios, it is necessary to delay the detachment of droplets from the solid surface. By increasing the contact time and contact area between the droplets and the solid surface, heat and mass transfer between the droplets and the solid can be enhanced. For example, by treating the surface of silk fabrics, the flow of ink droplets on silk from ink-jet printers can be suppressed, increasing the contact time and contact area, and enhancing the mass transfer efficiency of ink droplets on silk, thereby ultimately improving the image clarity of ink-jet printing.[4] Additionally, by using plasma etching to increase the surface texture of wool, the contact time between dye and wool can be prolonged, enhancing mass transfer between the dye and wool, and improving the ink-jet printing performance of wool fabrics.[5]

It is evident that the contact time and contact area have a major influence on the heat and mass transfer process between droplets and solids. Understanding the change rule of the contact time and contact area is therefore essential, and this motivates researchers to carry out a large number of studies to thoroughly examine the various factors affecting the contact time and contact area. For example, Abolghasemibizaki *et al.*[6] used extrusion-based three-dimensional (3D) printing technology to create macro-cylindrical ridges on the surface and studied this curved surface, the results showed that this surface would reduce the contact time between droplets and cylinders. Huang *et al.*[7] conducted experimental research to compare the dynamic behavior of droplet impacting on cylindrical superhydrophobic surfaces with and without grooves. The results indicated that, within specific Weber number ranges, the cylindrical surface with grooves reduced the contact time of droplets compared to a smooth cylindrical surface. Jin *et al.*[8] conducted experimental research on the impact and freezing processes of a water droplet on different cold cylindrical surfaces. The results showed that, during the impact process of the water droplet, the maximum contact diameter along azimuthal direction was generally larger than that along axial direction. Liu *et al.*[9] investigated the impact of Weber number and sphere-to-droplet diameter ratio on the collision between

[†]Corresponding author. E-mail: usstyf@126.com

© 2024 Chinese Physical Society and IOP Publishing Ltd

droplets and superhydrophobic spheres through experimental methods. The results indicated that, as the diameter ratio decreases, the contact time of droplets on the sphere consistently reduces. Lu *et al.*[10] studied the contact of sodium hydroxide emulsion droplets on coal surfaces using optical and high-speed video microscopes, the results showed that the contact time of emulsion droplets on coal surfaces was longer than that of crude oil. The above works were studied using experimental methods. Experimental methods have the advantages of being realistic and credible, but they also have the disadvantages of being time-consuming and costly. In contrast, numerical simulation methods have the advantages of being economical and efficient, therefore they have been increasingly widely applied in the study of droplet spreading phenomena on surfaces. Wang *et al.*[11] employed a particle-based mesh-free numerical approach to simulate and study the dynamic characteristics of droplets impacting on transmission lines with different wetting properties and sizes. The results indicated that droplet impacting on hydrophobic surfaces of transmission lines leads to a retraction of the contacting portion toward the center of the droplet, resulting in a continuously decreasing contact length. Wang *et al.*[12] employed a particle-based mesh-free numerical approach to simulate the impact of droplets on cylinders with different sizes and wettability. The results indicated that the length of the contacting portion increases with the enlargement of the cylinder size. Li *et al.*[13] employed a particle-based mesh-free numerical approach to simulate and investigate the dynamic behavior of droplet impacting on different sized superhydrophobic solid spheres. The results indicated that, during the droplet impact scenario, the contact time between the droplet and the sphere is significantly shorter compared to rebound situations. Luo *et al.*[14] investigated the maximum spreading length of droplets impacting cylindrical surfaces using numerical simulation and theoretical analysis. The results indicated that the maximum spreading length decreased with an increase in the contact angle. Luo *et al.*[15] employed Fluent software to study the mechanisms and parameters affecting the contact time of droplets impacting cylindrical surfaces. The results revealed that increasing the Weber number or reducing the cylinder diameter can effectively reduce the contact time. Shi *et al.*[16] proposed an analytical framework to study the impact and freezing delay of water droplets on hydrophobic solid surfaces below freezing point temperatures.

Originating in statistical mechanics, the lattice Boltzmann method has numerous advantages, including simplicity, efficiency, and ease of implementing boundary conditions.[17] Therefore, this method has been widely applied in areas including particle suspensions, non-Newtonian fluid flows, turbulence, natural convection, and heat and mass transfer.[18–22] Currently, the lattice Boltzmann method has mainly derived four multiphase flow models, including the pseudo-potential model,[23,24] the color-gradient model,[25,26] the phase field model,[27,28] and the free energy model.[29,30] Since the pseudo-potential model can directly calculate the interactive forces between fluids through the pseudo-potential, it can automatically track the movement of the interface between phases and has high computational efficiency. Therefore, the pseudo-potential model has been widely used in the study of multiphase flow problems.

For instance, Zhumatay *et al.*[31] used the multiphase Shan–Chen pseudo-potential lattice Boltzmann model to predict the contact time and gravity-driven displacement of immiscible droplets on surfaces with different wettability conditions. Tilehboni *et al.*[32] used the lattice Boltzmann method to simulate the process of gravity-induced droplet detachment from a wall. The results indicated that the contact time and length between the droplet and the wall varied due to the surface wettability. An *et al.*[33] simulated the separation process of low-salinity water and oil droplets with varying wettability. The results indicated that the diffusion length scale played a crucial role in the contact time. Furthermore, An *et al.*[34] proposed an improved multiple-relaxation-time pseudo-potential multiphase lattice Boltzmann model for studying binary droplet collisions at various collision angles. Lin *et al.*[35] employed the lattice Boltzmann pseudo-potential model to investigate the dynamic behavior of droplet impacting on superhydrophobic surfaces with rectangular ridges. The results indicated that superhydrophobic surfaces with rectangular ridges can effectively reduce the contact time with droplets. Zhang *et al.*[36] used the lattice Boltzmann method to investigate the dynamic behavior of droplet impacting on superhydrophobic cylindrical surfaces. The results indicated that as the Weber number increases, the contact time of the droplet continuously decreased. Zhang *et al.*[37] used the lattice Boltzmann method to investigate the influence of Weber number (We) and the cylinder-to-droplet radius ratio (R^*) on the dynamic behavior of low-viscosity droplets impacting hydrophobic cylinders. The results indicated that the contact time of droplets on the cylindrical surface decreased with an increase in R^* or a decrease in We. Zhang *et al.*[38] used the lattice Boltzmann method to conduct a comparative study on the dynamic behavior of low-viscosity droplets impacting smooth cylindrical surfaces and surfaces with ridges. The research results indicated that, compared to smooth cylindrical surfaces, the contact time of droplets on surfaces with ridges is significantly reduced. Chen *et al.*[39] used a lattice Boltzmann pseudo-potential model to simulate the merging and detachment process of two droplets on a cylindrical wall with a liquid–vapor density ratio of approximately 6 and distinct wettability gradients. The findings indicated that introducing wettability gradients on the cylindrical surface would accelerate the detachment of droplets.

It is worth pointing out that the equation of state utilized by Chen *et al.*[39] is based on the equation of state initially provided by Shan and Chen when they first proposed the pseudo-potential model.[23] This equation is not a genuine fluid equation of state, so it has limitations when dealing with two-phase flow problems involving large density ratios. The actual liquid–vapor density ratio is approximately 1000. Therefore, while simulating the motion of droplets on a solid surface, taking into account the properties of this noticeably large liquid–vapor density ratio will assist in obtaining computational results that are more following real-world situations.

To deeply understand the laws governing changes in droplet contact time and contact length during the contact process with solids, this paper employs a lattice Boltzmann pseudo-potential two-phase flow model. By introducing the non-ideal Peng–Robinson (PR) equation of state,[40] under the condition of considering a liquid–vapor density ratio of approximately 1000, the motion of a single droplet on the surface of a cylinder under the action of gravity is studied. The influences of several factors on the droplet contact length and contact time are analyzed.

2. Numerical method

2.1. Multiple-relaxation-time lattice Boltzmann pseudo-potential model

The fluid flow is simulated using the multi-relaxation-time lattice Boltzmann equation,[41] which evolution equation is

$$\begin{aligned} &f_\alpha(\boldsymbol{x}+\boldsymbol{e}_\alpha\delta_t, t+\delta_t) = f_\alpha(x,t) \\ &-(\boldsymbol{M}^{-1}\boldsymbol{\Lambda}\boldsymbol{M})_{\alpha\beta}(f_\beta - f_\beta^{\mathrm{eq}}) + \delta_t F'_\alpha, \end{aligned} \tag{1}$$

where f_α is the distribution function. f_α^{eq} is the equilibrium distribution function. δ_t is time step, it usually takes 1. $\boldsymbol{e}_\alpha$ is the discrete velocity in the α-direction. F'_α is the forcing term in the discrete velocity space. $\boldsymbol{M}$ is an orthogonal transformation matrix, and $\boldsymbol{\Lambda}$ is a diagonal matrix. Via the orthogonal transformation matrix $\boldsymbol{M}$, the right side of Eq. (1) can be written as

$$\boldsymbol{m}^* = \boldsymbol{m} - \boldsymbol{\Lambda}(\boldsymbol{m} - \boldsymbol{m}^{\mathrm{eq}}) + \delta_t\left(\boldsymbol{I} - \frac{\boldsymbol{\Lambda}}{2}\right)\boldsymbol{S}, \tag{2}$$

where, $\boldsymbol{m} = \boldsymbol{M}f$, $\boldsymbol{m}^{\mathrm{eq}} = \boldsymbol{M}f^{\mathrm{eq}}$, $\boldsymbol{I}$ is the unit matrix, $\boldsymbol{S}$ is the instantaneous spatial force term, and $(\boldsymbol{I} - 0.5\boldsymbol{\Lambda})\boldsymbol{S} = \boldsymbol{M}\boldsymbol{F}'$. Then, the multiple-relaxation-time lattice Boltzmann equation can be expressed as follows:

$$f_\alpha(\boldsymbol{x}+\boldsymbol{e}_\alpha\delta t, t+\delta t) = f_\alpha^*(\boldsymbol{x}, t), \tag{3}$$

where $f^* = \boldsymbol{M}^{-1}\boldsymbol{m}^*$. Equations (2) and (3) are respectively the collision and streaming processes in the LB equation. The diagonal matrix $\boldsymbol{\Lambda}$ includes the relaxation time and its expression is

$$\boldsymbol{\Lambda} = \mathrm{diag}(\tau_\rho^{-1}, \tau_{\mathrm{e}}^{-1}, \tau_\varsigma^{-1}, \tau_{\mathrm{j}}^{-1}, \tau_{\mathrm{q}}^{-1}, \tau_{\mathrm{j}}^{-1}, \tau_{\mathrm{q}}^{-1}, \tau_\nu^{-1}, \tau_\nu^{-1}). \tag{4}$$

The momentum balance matrix $\boldsymbol{m}^{\mathrm{eq}}$ is as follows:

$$\begin{aligned} \boldsymbol{m}^{\mathrm{eq}} = \rho(&1, -2+3|v|^2, 1-3|v|^2, v_x, \\ &-v_x, v_y, -v_y, v_x^2 - v_y^2, v_x v_y)^{\mathrm{T}}. \end{aligned} \tag{5}$$

where $\boldsymbol{v}$ is the macroscopic velocity and $|\boldsymbol{v}| = \sqrt{v_x^2 + v_y^2}$. The macro-density and macro-velocity are calculated as

$$\rho = \sum_\alpha f_\alpha, \rho\boldsymbol{v} = \sum_\alpha \boldsymbol{e}_\alpha f_\alpha + \frac{\delta t}{2}\boldsymbol{F}, \tag{6}$$

where $\boldsymbol{F} = (F_x, F_y)$ is the total force acting on fluid particles, which includes the fluid–fluid interaction force, $\boldsymbol{F}_{\mathrm{int}}$, the fluid–solid interaction force, $\boldsymbol{F}_{\mathrm{ads}}$, and other force, $\boldsymbol{F}_{\mathrm{b}}$.

$$\boldsymbol{F}_{\mathrm{int}} = -G\Psi(x)\sum_\alpha w_\alpha \Psi(\boldsymbol{x}+\boldsymbol{e}_\alpha)\boldsymbol{e}_\alpha, \tag{7}$$

where $\Psi(\boldsymbol{x}) = \sqrt{2(P_{\mathrm{EOS}} - \rho c_{\mathrm{s}}^2)/Gc^2}$, $\boldsymbol{G}$ is the contact strength, w_α is a weighting coefficient. To achieve thermodynamic consistency, the revised force source term $\boldsymbol{S}$ is as follows:[42]

$$\boldsymbol{S} = \begin{bmatrix} 0 \\ 6\boldsymbol{v}\cdot\boldsymbol{F} + \dfrac{12\sigma_\alpha|\boldsymbol{F}_\alpha|^2}{\psi^2\delta_t(\tau_{\mathrm{e}} - 0.5)} \\ -6\boldsymbol{v}\cdot\boldsymbol{F} - \dfrac{12\sigma_\alpha|\boldsymbol{F}_\alpha|^2}{\psi^2\delta_t(\tau_\zeta - 0.5)} \\ F_x \\ -F_x \\ F_y \\ -F_y \\ 2(v_xF_x - v_yF_y) \\ v_xF_y + v_yF_x \end{bmatrix}, \tag{8}$$

where σ_α is the variation to adjust the stability, $|\boldsymbol{F}|^2 = (F_x^2 + F_y^2)$, and F_{b} is as follows:

$$\boldsymbol{F}_{\mathrm{b}} = (\rho - \rho_{\mathrm{ave}})\boldsymbol{g}, \tag{9}$$

where ρ_{ave} is the average density in the calculation area. g is the gravitational acceleration. $\boldsymbol{F}_{\mathrm{ads}}$ is as follows:[43]

$$\boldsymbol{F}_{\mathrm{ads}} = -3G\psi(\rho(\boldsymbol{x},t))\sum_{i=1}^{8} w_\alpha \psi(\rho_{\mathrm{w}})s(\boldsymbol{x}+\boldsymbol{e}_\alpha\delta t)\boldsymbol{e}_\alpha, \tag{10}$$

where ρ_{w} is the virtual wall density. $s(\boldsymbol{x}+\boldsymbol{e}_\alpha\delta t)$ is an indicator function that is equal to 1 or 0 depending on whether the node is a solid or fluid domain node.

2.2. Peng–Robinson equation of state

The non-ideal Peng–Robinson equation of state can be written as follows:[40]

$$P_{\mathrm{EOS}} = \frac{\rho RT}{1-b\rho} - \frac{a\rho^2\varepsilon(T)}{1+2b\rho-b^2\rho^2}, \tag{11}$$

where $\varepsilon(T) = [1+(0.37464+1.54226\omega-0.26992\omega^2)(1-\sqrt{T/T_{\mathrm{c}}})]$, $a = 0.45724R^2T_{\mathrm{c}}^2/P_{\mathrm{c}}$, $b = 0.0778RT_{\mathrm{c}}/P_{\mathrm{c}}$, T_{c}, and P_{c} are critical temperature and critical pressure, respectively. This study sets $a = 0.06$, $b = 0.095$, $R = 1.0$, $T_{\mathrm{c}} = 0.0109383$, and $\omega = 0.344$. Furthermore, $T = 0.59T_{\mathrm{c}}$ was chosen to simulate the scenario with a high liquid–vapor density ratio. This corresponds to a liquid phase density of 8.7788 and a vapor phase density of 0.008608, resulting in a density ratio of 1019.8 between the liquid and vapor phases.

3. Physical model

The model of a droplet motion on a circular cylinder with wettability gradient is shown in Fig. 1. A rectangular area measuring 500 by 800 is used as the computing domain, and periodic boundary are implemented on all sides. A solid circular cylinder with a radius of $R = 100$ and a center at (250.1,600.1) is positioned in the upper portion of the rectangular region. A droplet with a radius of $r = 27$, tangent to the circular cylinder, is located in the top left portion of this cylinder and its point of tangency is located at coordinates (196.4,686.7). Furthermore, the cylinder's core angle increases counterclockwise, with 0° on the x axis.

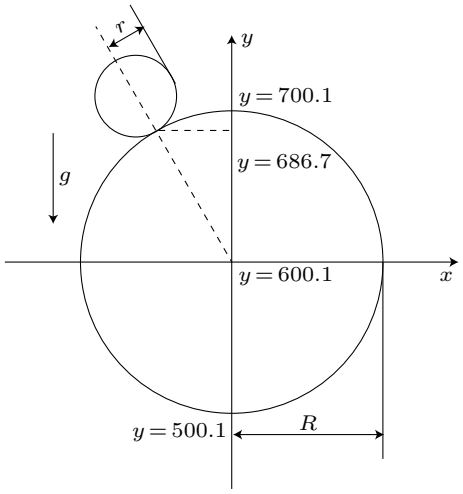


Fig. 1. Model of droplet motion on a circular cylinder with wettability gradient.

The cylindrical surface's contact angle distribution is symmetrically established along the y axis in the computation. With a contact angle of 150° at the point of tangency, the droplet is initially tangent to the cylinder. The contact angle is set to the minimum value of 75° at coordinates (250.1, 500.1), which correspond to the lowest point on the cylinder. The contact angle changes linearly along the y axis between these two positions. The contact angle measurements are then extrapolated over the whole left half-circle of the cylinder using this linear relationship. As a consequence, figure 2 illustrates the distribution of contact angles that result along the cylinder's left side along the y axis.

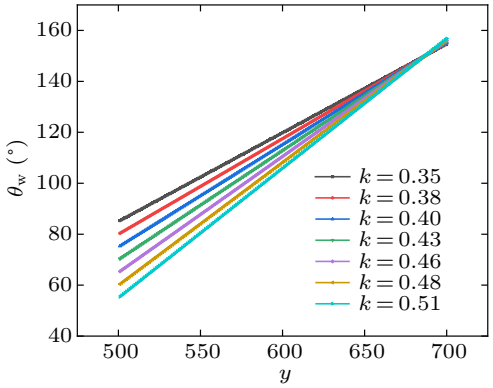


Fig. 2. Variation of wall wettability angle with the cylindrical surface's y coordinate.

The following expression was used to define the wettability gradient k:

$$k = \frac{150-75}{686.7-500.1}, \tag{12}$$

where the numerator of the right side of the equation represents the difference between the contact angle at the point of tangency and the contact angle at the lowest point of the cylinder. The denominator represents the difference in y coordinates between the point of tangency and the lowest point of the cylinder.

Equation (12) yields the computed value of $k = 0.40$. Similarly, multiple values of k can be achieved by altering the contact angle at the lowest point of the cylinder to different degrees while maintaining the contact angle at the point of tangency constant at 150°. Table 1 displays the corresponding relationship.

Table 1. Relationship between the contact angle at the lowest point of the cylinder and k.

The contact angle at the lowest point of the cylinder (°)	k
55	0.51
60	0.48
65	0.46
70	0.43
75	0.40
80	0.38
85	0.35

The Bond number (Bo), which denotes the ratio of surface tension to gravitational forces acting on the droplet, is the dimensionless number used in the computation. This is how it is expressed:

$$Bo = \frac{\rho g r^2}{\sigma}, \tag{13}$$

where ρ is the droplet density, g is the gravitational acceleration, r is the droplet radius, σ is the droplet's surface tension.

4. Results and discussion

4.1. The three stages of motion of droplet on the cylindrical surface

With $r = 27$, $Bo = 3.7$, and $k = 0.46$, figure 3 illustrates how the droplet's shape changes over time on the cylindrical surface. The droplet is tangent to the cylinder and above its left side at $t = 0$. After a while, at $t = 2000$, the droplet begins to spread bilaterally, creating two contact points at the top and bottom ends. The lower endpoint advances quickly and the top endpoint begins to move counterclockwise ahead in the subsequent period of $t = 2000$–4000, which causes the contact length to keep growing. Then, the left endpoint moves slowly forward during the period of $t = 4000$–17000, while the right endpoint moves quickly ahead, causing the contact length to grow once more. The droplet eventually detaches from the cylinder during the $t = 17000$–37000 period, as the left endpoint goes forward fast while the right endpoint practically stops moving forward. This results in a steady decrease in the contact length between the droplet and the cylinder.

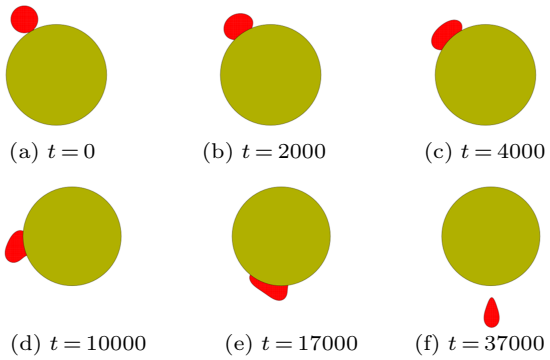


Fig. 3. Droplet morphology with time at conditions of $r = 27$, $Bo = 3.7$, and $k = 0.46$.

In order to analyze the motion of droplet on the cylinder, the droplet's contact time and contact length were studied. In this paper, the motion time of the droplet on the cylinder is defined as the contact time t_a. Since there are cases where the droplet adheres to the cylindrical surface all the time, we set the contact time for such cases to 60000, denoted as t, and define t_a/t as the relative contact time. The contact length L_a, which is represented by the ratio L_a/R, is the relative length of the contact region between the droplet and the cylindrical surface. As shown in Fig. 4, the two ends of the contact area correspond to the circular point and rectangular point on the cylinder, respectively, where the circular point is defined as the advancing point, with the corresponding central angle being θ_a; the rectangular point is defined as the receding point, with the corresponding central angle being θ_r.[44] Figure 5 shows the evolution of θ_a and θ_r with time during the process from the initial position of the droplet till it completely detaches from the cylindrical surface. It can be observed that θ_a first increases rapidly to the maximum value of 281°, then decreases slowly to 269°; while θ_r first decreases slowly to the minimum value of 112°, then increases rapidly to 269°, coinciding with θ_a.

By analyzing the evolution of θ_a and θ_r with time, the motion of the droplet can be divided into three stages: spreading, sliding, and aggregating. As depicted in Fig. 5, the spreading stage terminates when $\theta_r = (\theta_r)_{min}$, while the sliding stage terminates when $\theta_a = (\theta_a)_{max}$.

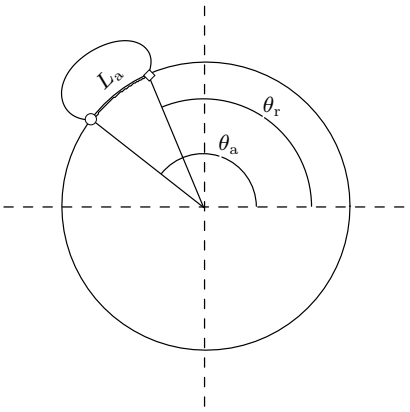


Fig. 4. Schematic of θ_a and θ_r.

Based on the data in Fig. 5, we calculated the evolution of L_a/R with time as the droplet moved from its initial position until completely detaching from the cylindrical surface. The results are depicted in Fig. 6. According to the corresponding moments in Fig. 5, we have divided the entire motion of the droplet into three stages: spreading, sliding, and aggregating, represented respectively by dashed lines, solid lines, and dotted lines. The following conclusions can be drawn from Fig. 6: in the spreading stage, L_a/R rapidly increases, reaching 0.22; in the sliding stage, L_a/R first rises to 0.29, then slowly decreases to 0.25, followed by another rapid increase, ultimately reaching a maximum value of 0.41; whereas in the aggregating stage, L_a/R continuously decreases, eventually approaching 0, indicating the droplet has completely detached from the cylindrical surface.

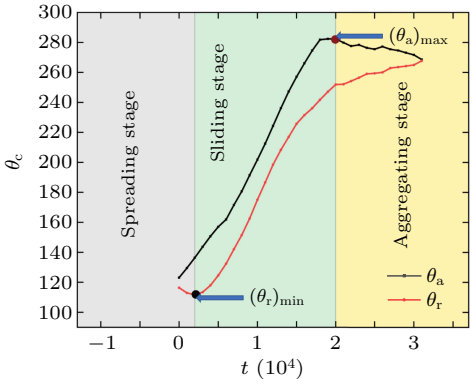


Fig. 5. Evolution of θ_a and θ_r with time.

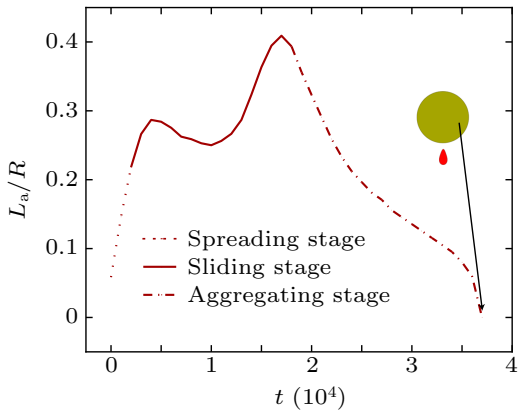


Fig. 6. Evolution of L_a/R with time at operating conditions of $r = 27$, $Bo = 3.7$, and $k = 0.46$.

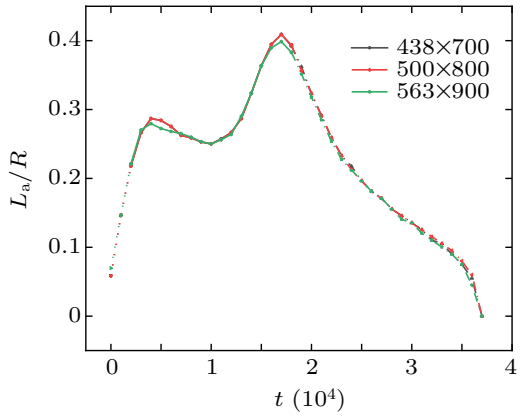


Fig. 7. Grid independence verification.

In the case of $r = 27$, $Bo = 3.7$, and $k = 0.46$, the grid-independent verification is performed for the evolution of L_a/R with time using three grid resolutions of 438×700, 500×800, and 563×900, and the results are presented in Fig. 7. It is evident from Fig. 7 that, for different grid resolution, the variation trend of L_a/R is highly similar. Moreover, the root mean square error (RMSE) is used to characterize the accuracy of the results of different grid calculations. The expression formula for RMSE is shown below:

$$\mathrm{RMSE} = \sqrt{\frac{1}{n}\sum_{n}[(L_a/R)_i - (L_a/R)_j]^2}, \tag{14}$$

where n is the number of samples taken, i, j are case numbers and $j = 1$.

The results of RMSE are shown in Table 2. It can be seen that the maximum RMSE error is only 0.557%, which fully satisfies the grid-independence requirement. Therefore, the grid resolution of 500×800 is reasonable.

Table 2. Results of RMSE for different grid resolution.

Case number	Grid resolution	RMSE (%)
1	500×800	
2	438×700	0.209
3	563×900	0.557

4.2. Effect of wettability gradient on relative contact length and contact time

We altered the value of k and monitored the droplet morphology at different time, with $Bo = 3.7$ and $r = 27$. The computed results are displayed in Fig. 8. The droplet is depicted in the illustration as it descends along the cylinder, changing shape continuously. When the droplet finally reaches the bottom of the cylinder, it may cling to the cylinder's surface or it may separate from it. To be more precise, the droplet will adhere to the cylinder surface when $k \geq 0.48$ and separate from it when $k \leq 0.46$.

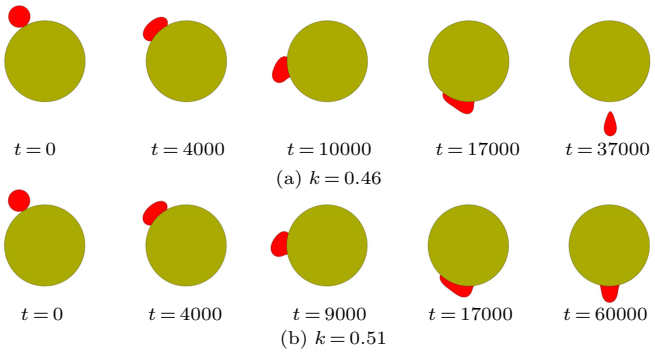


Fig. 8. Impact of the wettability gradient on the motion of droplets at operating conditions of $r = 27$, $Bo = 3.7$.

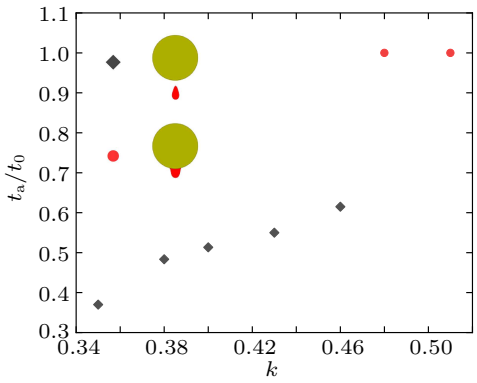


Fig. 9. Relationship of t_a/t with k at operating conditions of $r = 27$, $Bo = 3.7$.

To further analyze the motion of droplets on the cylindrical wall surface under different k values, we studied the relative contact time t_a/t and the relationship between the relative contact length L_a/R and time under different k values. First, we studied the relationship between t_a/t and k. The results are shown in Fig. 9. It is evident that t_a/t likewise increases steadily with k. t_a/t develops very slowly when k is between 0.34 and 0.46; fast when k is larger than 0.46 and less than 0.48, and the droplet attaches to the cylinder surface when k is greater than or equal to 0.48.

We then looked at the relationship, for various values of k, between L_a/R and time. Figure 10 presents the findings. The spreading and sliding stages correspond to similar changes in L_a/R throughout time. There are two situations for L_a/R in the aggregating stage: The droplet adheres to the cylinder surface when k is greater than or equal to 0.48, as indicated by

the blue and green lines in the figure; when k is less than or equal to 0.46, as indicated by the black and red lines in the figure, the droplet separates from the cylinder surface and the final L_a/R becomes zero.

Finally, we analyzed the relationship between $(L_a/R)_{max}$ and various values of k obtained from Fig. 10. It is evident from Fig. 11 that $(L_a/R)_{max}$ progressively rises from 0.22 to 0.44 when k falls between 0.35 and 0.51. $(L_a/R)_{max}$ likewise steadily rises as k grows, until reaching the maximum value of 0.44.

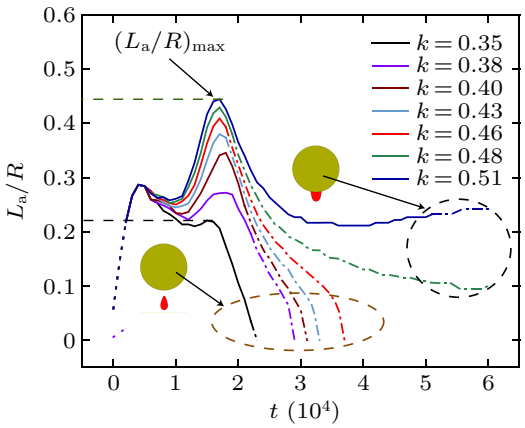


Fig. 10. Evolution of L_a/R with time for various values of k at operating conditions of $r = 27$, $Bo = 3.7$.

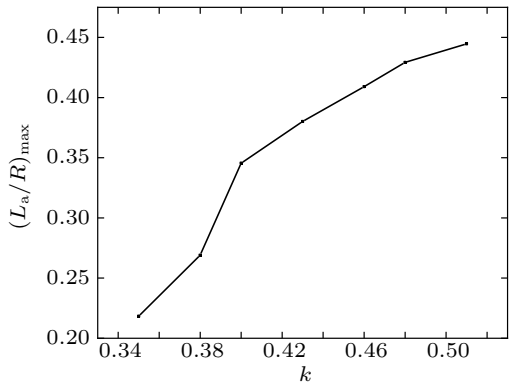


Fig. 11. Relationship of $(L_a/R)_{max}$ with k at operating conditions of $r = 27$, $Bo = 3.7$.

4.3. Effect of Bond numbers on relative contact length and contact time

We altered the value of Bo and monitored the droplet morphology at different times, with $k = 0.40$ and $r = 27$. The computed results are displayed in Fig. 12. The droplet's shape continuously changes as it descends along the cylinder. When the droplet finally reaches the bottom of the cylinder, it may cling to the cylinder's surface or it may separate from it. To be more precise, the droplet will adhere to the cylinder surface when $Bo = 3.1$ and separate from it when $Bo \geq 3.3$.

To further analyze the motion of droplets on the cylindrical wall surface under different Bo values, we studied the relative contact time t_a/t and the relationship between the relative contact length L_a/R and time under different Bo values. First, we studied the relationship between t_a/t and Bo. The results are shown in Fig. 13. It is evident that as the Bo value increases, t_a/t decreases continuously. When the Bo value is between 3.1 and 3.3, t_a/t drops rapidly; while when the Bo value is greater than 3.3 and less than 4.0, t_a/t drops slowly; when the Bo value is 3.1, the droplet attaches to the cylinder surface.

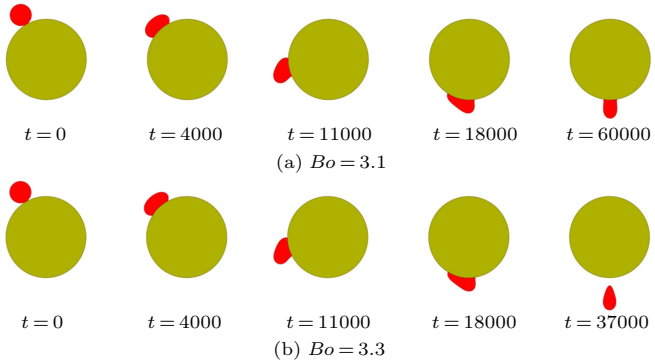


Fig. 12. Impact of Bo numbers on the motion of droplets at operating conditions of $r = 27$, $k = 0.40$.

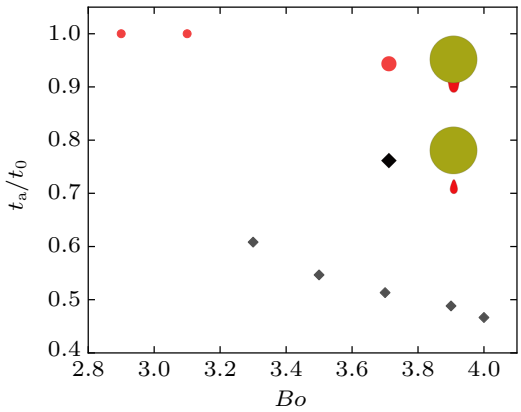


Fig. 13. Relationship of t_a/t with Bo at operating conditions of $r = 27$, $k = 0.40$.

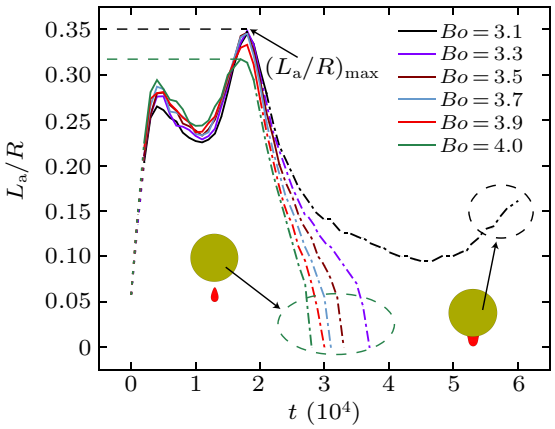


Fig. 14. Evolution of L_a/R with time for various values of Bo at operating conditions of $r = 27$, $k = 0.40$.

We then looked at the relationship between L_a/R and time under different Bo values. Figure 14 presents the findings. The trend of L_a/R changes over time in both the spreading and sliding stages is comparable under varying Bo values. There are two situations for L_a/R in the aggregating stage: The droplet

adheres to the cylinder surface when $Bo = 3.1$, as indicated by the black line in the figure; when Bo is greater than or equal to 3.3, as indicated by the green to purple lines in the figure, the droplet separates from the cylinder surface and the final L_a/R becomes zero.

Finally, we studied the relationship between $(L_a/R)_{max}$ and Bo values obtained from Fig. 14. It can be seen from Fig. 15 that when Bo ranges from 3.1 to 4.0, $(L_a/R)_{max}$ first slowly increases to the maximum value of 0.35, then gradually decreases, and finally rapidly drops to the minimum value of 0.32. As Bo increases, $(L_a/R)_{max}$ first increases and then decreases.

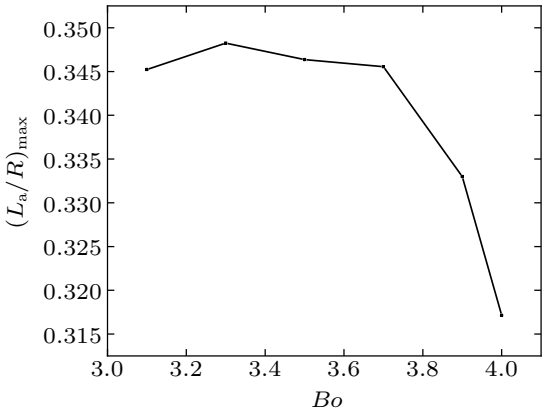


Fig. 15. Relationship of $(L_a/R)_{max}$ with Bo at operating conditions of $r = 27$, $k = 0.40$.

4.4. Effect of droplet radius on relative contact length and contact time

We altered the value of r and monitored the droplet morphology at different time, with $k = 0.40$ and $Bo = 3.7$. The computed results are displayed in Fig. 16. The droplet's shape varies as it descends the cylinder. When the droplet eventually reaches the bottom of the cylinder, it might adhere to the surface of the cylinder or it may come away from it. More precisely, at $r = 25.5$ the droplet will stick to the cylinder surface while at $r \geq 25.8$ it will detach from it.

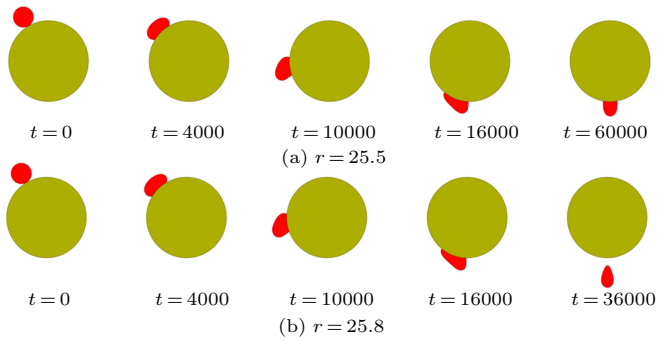


Fig. 16. Impact of droplet radius on the motion of droplets at operating conditions of $k = 0.40$, $Bo = 3.7$.

To further analyze the motion of droplets on the cylindrical wall surface under different r values, we studied the relative contact time t_a/t and the relationship between the relative contact length L_a/R and time under different r values. First, we studied the relationship between t_a/t and r. The results are shown in Fig. 17. It is evident that as r increases, t_a/t gradually decreases. Specifically, when r is between 25.5 and 25.8, t_a/t decreases rapidly; when r is greater than or equal to 25.8 and less than 27.3, the decreasing rate of t_a/t slows down; when $r = 25.5$, the droplet attaches to the cylinder surface.

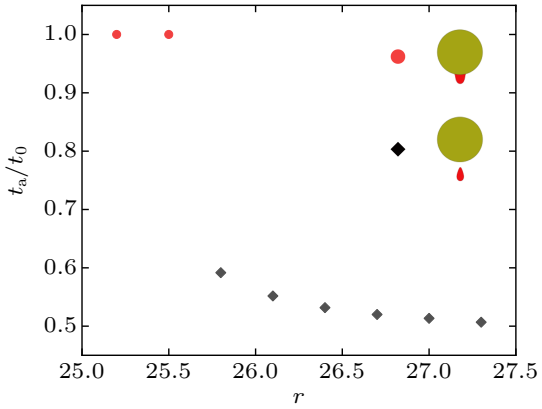


Fig. 17. Relationship of t_a/t with r at operating conditions of $k = 0.40$, $Bo = 3.7$.

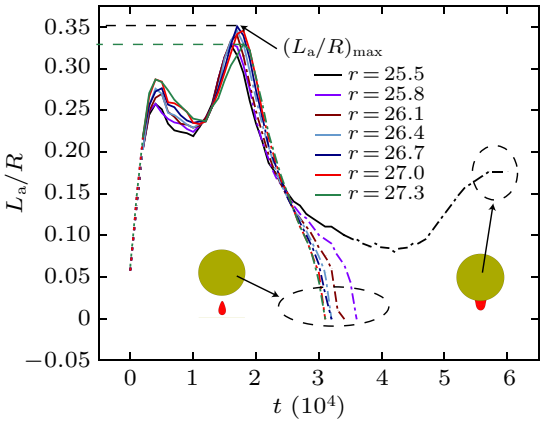


Fig. 18. Evolution of L_a/R with time for various values of$r$ at operating conditions of $k = 0.40$, $Bo = 3.7$.

We then looked at the relationship between L_a/R and time under different r values. Figure 18 presents the findings. The shifting trends of L_a/R over time in the spreading and sliding stages are comparable, regardless of how r varies. There are two scenarios in which the L_a/R changes during the accumulation stage: when $r = 25.5$ (the black line), the droplet adheres to the cylinder surface and the final L_a/R is not zero; when r is greater than or equal to 25.8 (the green to purple lines), the droplet separates from the cylinder surface and the final L_a/R is zero.

Finally, we analyzed the relationship between $(L_a/R)_{max}$ and r values obtained from Fig. 18. It is evident from Fig. 19 that when r falls between 25.5 and 26.7, $(L_a/R)_{max}$ rises with r, ultimately reaching the maximum value of 0.35; conversely, when r falls between 26.7 and 27.3, $(L_a/R)_{max}$ falls with r. As r increases, $(L_a/R)_{max}$ increases first and thereafter declines.

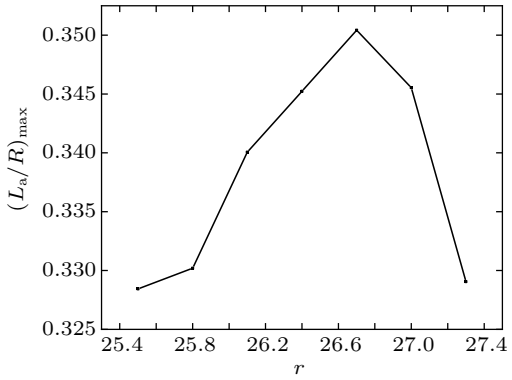


Fig. 19. Relationship of $(L_a/R)_{max}$ with r at operating conditions of $k = 0.40$, $Bo = 3.7$.

4.5. Phase diagrams of t_a/t and $(L_a/R)_{max}$ with k and Bo for three values of r

As was previously mentioned, the contact time and contact length are two crucial variables affecting the efficiency of heat and mass transfer. Longer contact periods and longer contact lengths can improve the efficiency of heat and mass transfer between the droplet and cylinder. Phase diagrams illustrating the variation of the droplet's maximum relative attachment length and relative attachment time with k and Bo for three values of r are given in this work.

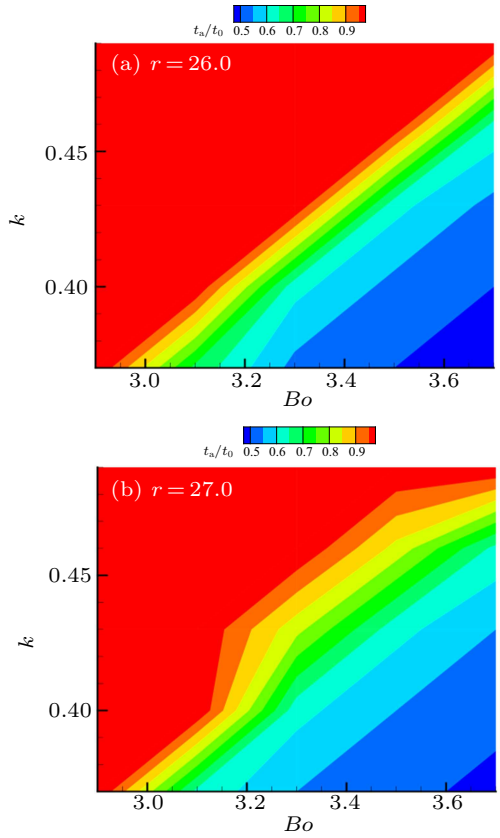


Fig. 20. Phase diagrams of (t_a/t) with k and Bo for three values of r.

Figures 20 and 21 show that the range of Bo is 2.9 to 3.7 with a 0.05 interval and the range of k is 0.37 to 0.49 with a 0.01 interval. The droplet in Fig. 20 is attached to the cylinder surface when it is red; when it is detached from the surface, it is indicated by various colors. The situation where the contact time steadily reduces is represented by the red-to-blue transition area. The contact time continuously decreases with the decrease of k. when Bo is held constant, and it likewise continuously decreases with the increase of Bo when k is held constant. The smallest contact length is shown by the blue area in Fig. 21, the largest contact length is shown by the red area, and the green area is longer than the blue area. The progressive increase in contact duration is represented by the blue to red transition. The contact length rises steadily as k increases while holding Bo constant. Eventually, when both k and Bo take the maximum values, the maximum contact length can be found.

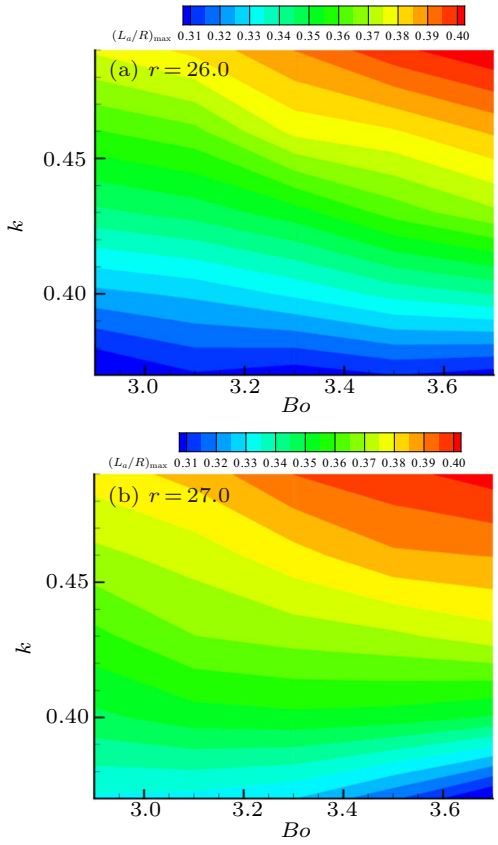


Fig. 21. Phase diagrams of $(L_a/R)_{max}$ with k and Bo for three values of r.

Additionally, we summarized in Figs. 20 and 21 the maximum and minimum values of t_a/t and $(L_a/R)_{max}$. The results are displayed in Tables 3 and 4. It is evident that when r grows, the minimum value of t_a/t rises, the maximum value of $(L_a/R)_{max}$ increases, and the minimum value of $(L_a/R)_{max}$ falls.

Table 3. The maximum and minimum values of t_a/t_0 of Fig. 19.

r	Minimum values of (t_a/t_0)	Maximum values of (t_a/t_0)
26.0	0.458	1.0
26.25	0.463	1.0
26.5	0.468	1.0
26.75	0.472	1.0
27.0	0.483	1.0

Table 4. The maximum and minimum values of $(L_a/R)_{max}$ of Fig. 20.

r	Minimum values of $(L_a/R)_{max}$	Maximum values of $(L_a/R)_{max}$
26.0	0.304	0.405
26.25	0.300	0.412
26.5	0.289	0.417
26.75	0.275	0.429
27.0	0.257	0.435

5. Conclusions

In this paper, a pseudo-potential lattice Boltzmann high-density ratio multiphase model was adopted to simulate the motion of a droplet on a circular cylindrical surface under gravity, and the following conclusions were obtained:

(i) The spreading process of the droplet on the cylinder can be divided into three stages: spreading, sliding, and aggregating, based on the time points corresponding to the extremum points during the changing process of θ_a and θ_r throughout time.

(ii) The relative contact time t_a/t and maximum relative contact length $(L_a/R)_{max}$ of the droplet exhibit different changing trends influenced by the wettability gradient (k), Bond number (Bo), and droplet radius (r). We found that, within the study's calculation range, t_a/t grows as k increases, lowers as Bo increases, and decreases as r increases. When k rises, $(L_a/R)_{max}$ increases as well; when Bo increases, it first increases and then drops, and when r increases, it first increases and then decreases.

(iii) With an increase in Bo and a decrease in k, the droplets can be removed from the cylinder surface more quickly when r remains constant. In the meantime, it appears that the droplets can achieve a longer attachment length due to the increases in Bo and k.

(iv) These findings offer useful references for fully comprehending droplet motion on cylindrical surfaces and maximizing the effectiveness of mass and heat transmission.

References

[1] Sayyari J M, Naghedifar A S and Esfahani J A 2020 *J. Braz. Soc. Mech. Sci. Eng.* **42** 142
[2] Xu B, Min S Q, Pan D, Ni J C and Zhang Y J 2023 *Colloids Surf. A* **675** 131974
[3] Li S P, Lai S J, Zhang R H and Guo Z G 2023 *Chem. Eng. J.* **470** 143659
[4] Liu K Q, Fang K J, Chen W C, Zhang C M, Sun L Y and Zhu J L 2023 *Int. J. Biol. Macromol.* **224** 1252
[5] Wang M Y, Shi F R, Zhao H Z, Sun F Y, Fang K J, Miao D G, Zhao Z H, Xie R Y and Chen W C 2022 *J. Cleaner Prod.* **362** 132333
[6] Abolghasemibizaki M, McMasters R L and Mohammadi R 2018 *J. Colloid Interface Sci.* **521** 17
[7] Huang C, Qian L J, Lv L, Huo B J, Zhu W and Wang Y S 2023 *Exp. Therm. Fluid Sci.* **144** 110867
[8] Jin Z Y, Zhang H H and Yang Z G 2017 *Int. J. Heat Mass Transfer* **113** 318
[9] Liu X, Min J C, Zhang X, Hu Z F and Wu X M 2021 *Int. J. Multiphase Flow* **141** 103675
[10] Lu Y, Wang X M, Liu W P, Li E Z, Cheng F Q and Miller J D 2019 *Fuel* **253** 273
[11] Wang Y L 2020 *Appl. Surf. Sci.* **516** 146155
[12] Wang Y L, Wang Y X and Wang S R 2020 *J. Colloid Sci.* **578** 207
[13] Li X X, Li H W, Zheng D and Wang Y X 2021 *Colloids Surf. A* **618** 126493
[14] Luo J, Wu S Y, Xiao L and Chen Z L 2021 *Int. J. Multiphase Flow* **143** 103774
[15] Luo J, Wu S Y, Xiao L and Chen Z L 2021 *Int. J. Mech. Sci.* **197** 106333
[16] Shi K W, Huang J X and Duan X L 2024 *Int. J. Therm. Sci.* **196** 108726
[17] Gai S L, Peng Z B, Moghtaderi B, Yu J L and Doroodchi E 2022 *Comput. Fluids* **246** 105616
[18] Chai Z H, Guo X Y, Wang L and Shi B C 2019 *Phys. Rev. E* **99** 023312
[19] Yang F, Yang H C, Yan Y H, Guo X Y, Dai R and Liu C Q 2017 *J. Mech. Sci. Technol.* **31** 3053
[20] Wang N N, Liu H H and Zhang C H 2017 *J. Rheol.* **61** 741
[21] Huang H B, Yang X, Krafczyk M and Lu X Y 2012 *J. Fluid Mech.* **692** 369
[22] Huang H B, Yang X and Lu X Y 2014 *Phys. Fluids* **26** 053302
[23] Shan X and Chen H 1993 *Phys. Rev. E* **47** 1815
[24] Chen W Y, Yang F, Yan Y H, Guo X Y, Dai R and Cai X S 2018 *J. Mech. Sci. Technol.* **32** 2637
[25] Gunstensen A K, Rothman D H, Zaleski S and Zanetti G 1991 *Phys. Rev. A* **43** 4320
[26] Yang F, Shao X S, Wang Y, Lu Y S and Cai X S 2021 *Eur. J. Mech. B. Fluids* **86** 90
[27] He X, Chen S and Doolen G D 1998 *J. Comput. Phys.* **146** 282
[28] Sun M Y, Ang L, Zhang X J, Fei Y X, Zhu L and Huang Z 2023 *J. Power Sources* **587** 233700
[29] Swift M R, Orlandini E, Osborn W R and Yeomans J M 1996 *Phys. Rev. E* **54** 5041
[30] Gong J M, Oshima N and Tabe Y 2019 *Comput. Math. Appl.* **78** 1166
[31] Zhumatay N, Kabdenova B, Monaco E and Rojas-solorzano L R 2021 *Eur. J. Mech. B. Fluids* **86** 198
[32] Tilehboni S E M, Fattahi E, Afrouzi H H and Farhadi M 2015 *J. Mol. Liq.* **212** 544
[33] An S Y, Zhan Y T, Mahani H and Niasar V 2022 *Fuel* **329** 125294
[34] An X, Dong B, Li W Z, Zhou X and Sun T 2021 *Comput. Math. Appl.* **92** 76
[35] Lin D J, Wang L, Wang X D and Yan W M 2019 *Int. J. Heat Mass Transfer* **132** 1105
[36] Zhang L Z, Wang Y B, Gao S R, Lin D J, Yang Y R, Wang X D and Lee D J 2021 *J. Taiwan Inst. Chem. Eng.* **126** 359
[37] Zhang L Z, Xu S Y, Wang Y F, Yang Y R, Zheng S F, Gao S R, Wang X D and Lee D J 2022 *Langmuir* **38** 11860
[38] Zhang L Z, Chen X, Yang Y R and Wang X D 2023 *Langmuir* **39** 6375
[39] Chen L, Gao M, Liang J, Wang D M, Hao L and Zhang L X 2022 *Eng. Appl. Comp. Fluid* **16** 1796
[40] Gong S and Cheng P 2015 *Int. J. Heat Mass Transfer* **80** 206
[41] Arsalan H, Abdolrahman D, Sajad R and Keivan M 2023 *Theor. Comput. Fluid Dyn.* **37** 83
[42] Li Q, Luo K H and Li X J 2013 *Phys. Rev. E* **87** 053301
[43] Yao J, Wang J F, Dong Q M, Wang D B, Zhang W, Xu H J and Zuo L 2022 *Appl. Therm. Eng.* **211** 118517
[44] Zhang K X, Zhao J Y, Chen S, Wang Y X and Liu Y 2019 *Appl. Surf. Sci.* **486** 337